Assessment of Scatter Compensation Strategies for ^{67}Ga SPECT Using Numerical Observers and Human LROC Studies

Troy H. Farncombe, PhD[1]; Howard C. Gifford, PhD[2]; Manoj V. Narayanan, PhD[3]; P. Hendrik Pretorius, PhD[2]; Eric C. Frey, PhD[4]; and Michael A. King, PhD[2]

[1]Department of Nuclear Medicine, Hamilton Health Sciences Center, Hamilton, Ontario, Canada; [2]Division of Nuclear Medicine, Department of Radiology, University of Massachusetts Medical School, Worcester, Massachusetts; [3]CPS Innovations, Knoxville, Tennessee; and [4]Department of Radiology, Johns Hopkins University, Baltimore, Maryland

^{67}Ga citrate is an oncologic SPECT imaging agent often used to diagnose or stage patients with non-Hodgkin's lymphoma. As ^{67}Ga decay involves the emission of multiple-energy γ-rays, significant photon downscatter will be present within each photopeak energy window. We have previously shown that the inclusion of these scattered photons significantly degrades lesion detectability. The goal of this study was to investigate the extent to which this decrease in detectability can be reversed by applying scatter compensation strategies. **Methods:** We have compared 5 different scatter compensation methods to the case of no scatter compensation in iterative SPECT image reconstruction. The strategies consisted of (a) perfect scatter rejection, (b) ideal scatter compensation, (c) triple-energy window (TEW) scatter estimation, (d) effective scatter source estimation (ESSE), and (e) postreconstruction scatter subtraction. Reconstruction parameters used for each method were first optimized using a channelized Hotelling numerical observer. Strategies were then ranked in terms of lesion detectability using a human observer localization receiver operating characteristic (LROC) study. An additional comparison was made comparing the human LROC rankings with a recently developed channelized nonprewhitening (CNPW) LROC numerical observer. **Results:** Using the area-under-the-LROC-curve (A_{LROC}) as the assessment criterion, our results indicate that the TEW and ESSE scatter compensation methods are able to significantly improve lesion detectability over no compensation (A_{LROC} = 0.75 and 0.73 vs. 0.67, respectively). However, these compensations failed to achieve the same detectability as perfect scatter rejection (A_{LROC} = 0.84). Both ideal scatter compensation and postreconstruction scatter subtraction resulted in numerical increases in detection accuracy that were not statistically significant from no scatter compensation. Good agreement is seen between the CNPW observer and human LROC studies (Spearman rank order coefficient, r_s = 0.74), thus indicating that the LROC observer may be a good predictor of human observer performance in ^{67}Ga SPECT. **Conclusion:** Scatter compensation in ^{67}Ga SPECT imaging using techniques such as TEW or ESSE is able to improve lesion detectability compared with no scatter compensation. A recently developed numerical observer model appears to be a good predictor of human observer performance and may be used to perform imaging optimizations, thereby reducing the need for human LROC studies.

Key Words: ^{67}Ga SPECT; scatter compensation; localization receiver operating characteristic studies; numerical observer

J Nucl Med 2004; 45:802–812

In SPECT imaging, the addition of scattered photons into the photopeak energy acquisition window is responsible for degrading tumor contrast and the signal-to-noise ratio (*1*). Proper compensation for these photons must be performed if accurate attenuation compensation is to be performed (*2*,*3*). Possible gains in contrast made by incorporating scatter compensation typically are accompanied by altered noise characteristics; thus, the overall benefit of scatter correction for the task of lesion detection is uncertain.

Current methods of scatter compensation can generally be divided into 2 different categories (*4*,*5*) comprised of (a) those that estimate the scatter contributions to the projection data and then compensate for this contribution either before, during, or after reconstruction (*6–9*); and (b) those that model the scatter response function (SRF) during the reconstruction process (*10–13*).

Scatter estimation methods that fall into the first category can be performed using information acquired with additional energy windows (*6*,*8*) or by combining the acquired emission data with approximations to the SRF to estimate the scatter distribution in the projections (*7*). For each photon that is detected by a γ-camera, the apparent total energy deposited from this incident photon is known. However, due to the finite energy resolution of the detectors used in γ-cameras, the detected energy will not necessarily be the

Received Sep. 17, 2003; revision accepted Dec. 2003.

For correspondence or reprints contact: Troy H. Farncombe, PhD, Department of Nuclear Medicine, Room 1P14, Hamilton Health Sciences Center, 1200 Main St. W. Hamilton, ON, Canada, L8N 3Z5.

E-mail: farncomb@hhsc.ca.

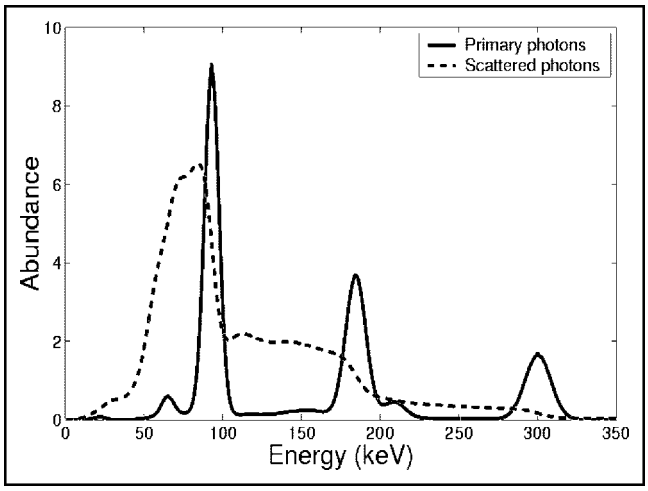

FIGURE 1. Simulated energy spectrums for detection of ^{67}Ga obtained using NaI(Tl) scintillator. Spectrums were obtained using the SIMIND Monte Carlo program.

same as the true photon energy. For NaI(Tl) scintillators this energy resolution is typically gaussian distributed and has a full width at half maximum (FWHM) of about 10% at 140 keV (Fig. 1). In comparison, solid-state detectors such as cadmium zinc telluride have energy resolution more on the order of 3%–6% and thus reduce the acquisition of scattered photons using correspondingly narrower photopeak energy windows. In the extreme case of perfect energy resolution, the photopeak window can be narrowed to the point of effectively rejecting all scatter events at the time of acquisition. Using the acquired energy spectrum obtained during imaging with NaI scintillation detectors, several scatter compensation methods have been proposed that attempt to achieve ideal scatter rejection by estimating the contribution of scatter within the photopeak energy windows, thereby reducing the influence of scattered photons in the reconstruction process. Examples of these approaches include: the triple-energy window (TEW) method (*8*), holospectral methods (*14*), neural networks (*15*), or the Compton window subtraction method (*6*) and similar variants. The main advantages of such methods are their speed and simplicity for clinical use.

As an alternative to the scatter estimation methods, reconstruction-based scatter compensation (RBSC) methods also exist. With this category, scatter compensation is achieved by mapping scattered photons back to their point of origin within the object being imaged (*5*). RBSC methods make use of all acquired photons and thus it has been argued that there should be less noise increase compared with the other category of compensation (*4,5*). Examples of this type of reconstruction strategy include Monte Carlo methods (*10,16,17*), analytic methods (*18*), and the effective scatter source estimation (ESSE) method (*13*). These methods are typically far more complex than the scatter-estimation methods and are therefore quite computationally intensive, thus rendering many of the methods infeasible in a clinical environment. Recent improvements on these methods have recently been developed, however, which dramatically reduce this processing time burden (*5,19–21*).

Beekman et al. (*12*) have previously compared for ^{99m}Tc-based tracers the methods of ideal scatter rejection (i.e., the imaging of solely primary photons), ideal scatter estimation (i.e., using the actual scatter content within each projection bin), and ideal scatter modeling (i.e., using perfect knowledge of the actual SRFs). This study determined that ideal scatter rejection achieved the highest contrast-to-noise ratio, followed by ideal scatter modeling and ideal scatter estimation. Similar results were reported by Kadrmas et al. (*5*) for ^{201}Tl cardiac imaging. However, Kadrmas et al. noted that they had not performed a study of differences among noise correlations between methods and that "such differences would be expected to affect the usefulness of reconstructed images for tasks such as lesion detection" (*5*). Thus human-observer lesion detection studies are needed to assess the impact on lesion detectability of these different types of scatter compensation strategies.

de Vries et al. (*22,23*) investigated the impact of scatter on cold and hot lesion detection for ^{99m}Tc-labeled antibody fragments used in hepatic SPECT imaging. Analysis was made of the impact of dual-photopeak window (DPW) scatter compensation in Monte Carlo simulated projections with the appropriate level of scatter for ^{99m}Tc and using an approximation for ^{67}Ga in which 2.5 times the scattered ^{99m}Tc photons were present. A signal-known-exactly receiver-operating-characteristic (SKE-ROC) study was conducted in which the potential location of the lesion was indicated via removable crosshairs to 5 observers who recorded their confidence as to lesion presence on a continuous rating scale. The area-under-the-ROC-curve (A_z) of a binomial model ROC curve fit to each observer's rating data was used to compare compensation strategies. Statistical analysis of the A_z's indicated that only for the case of the hot tumors was there any significant difference in detectability between ideal scatter rejection and no compensation at all. In the case of artificially high scatter content, primary photon–only images gave a significant increase in detectability for both tumor types (0.88 vs. 0.81 for cold, and 0.84 vs. 0.74 for hot). In no case, however, did the investigated scatter compensation method result in a statistically significant increase in detectability over that of no compensation. However, there was a numerical increase in the observer averaged A_z's for the high-scatter case with scatter compensation compared with no compensation for both polarities (0.83 vs. 0.81 for cold, and 0.78 vs. 0.74 for hot), indicating a possible improvement in detectability with scatter compensation. As mentioned, one of the drawbacks to this investigation was that the high scatter content was obtained by simply increasing the standard ^{99m}Tc scatter distribution within the 140-keV photopeak by a factor of 2.5, thereby not accurately representing SPECT imaging with ^{67}Ga. Another drawback was that DPW scatter compensation was the only compensation method investigated.

Additionally, to obtain A_z values near the desired range of between 0.75 and 0.80 (*24*) while still keeping the number of acquired counts clinically relevant, the simulated lesion contrast had to be reduced to well below that which would be reported as having been detected clinically, thus resulting in a difficult extrapolation of results to clinical studies. Finally, an SKE-ROC paradigm was used whereby the location of the simulated tumor was indicated to the observers rather than incorporating the lesion search task as part of the lesion detection problem as would be performed in localization ROC (LROC).

In this study we investigated the potential improvement in lesion detection on application of selected scatter compensation strategies for ^{67}Ga citrate SPECT imaging. ^{67}Ga citrate imaging was selected as the vehicle for these investigations as a result of its clinical significance and the large impact of photon scatter (*1*). This radionuclide decays via the emission of multiple energy γ-rays (Table 1) and thus introduces complications in imaging due to the likelihood of high-energy photons undergoing large-angle scatters and being detected within lower-energy acquisition windows.

We have selected to use an iterative image reconstruction algorithm as we have seen improved lesion detection accuracy resulting from the use of these algorithms compared with filtered backprojection (*25*). Five scatter compensation strategies consisting of both scatter estimation and RBSC types are compared using both numerical and human observers for the tasks of localizing and detecting simulated tumors.

In the past, we have observed very good agreement in the relative rankings of different SPECT reconstruction strategies when using a signal-known-exactly background-known-exactly (SKE-BKE) channelized Hotelling observer (CHO) and human observers performing LROC studies (*26*,*27*). However, due to the lack of localization information available with the SKE-CHO, there exists a potential source of disagreement between the CHO and LROC results as the CHO is provided with information on the exact lesion location and, as such, does not tend to get tricked by other sources of activity within the image. Though it is possible to devise a location-averaged CHO, the computation of such an observer model would require a very large number of images to be created and processed if sample statistics are to be used. To ease this large computational burden, alternative methods have been used to estimate population statistics from noise-free images (*28*), but potential difficulties may still exist when directly comparing results from the 2 types of observer studies.

TABLE 1
^{67}Ga Emission Energies and Decay Abundance

Energy (keV)	Abundance (%)	Energy (keV)	Abundance (%)
91.3	3.2	393.5	4.7
93.3	39.2	494.7	<1
184.6	21.2	703.1	<1
209.0	2.4	794.4	<1
300.2	16.8	887.7	<1

Recently, Gifford et al. (*29*,*30*) have developed a channelized nonprewhitening (CNPW) numerical observer that includes a lesion localization task with the goal of better modeling human observer performance and thus being able to obtain greater statistical power when comparing image reconstruction strategies. Thus, in addition to measuring the performances of various scatter compensation strategies, a secondary goal of this investigation was to determine the extent of agreement of this CNPW observer with human observers in the ranking of selected scatter compensation strategies.

MATERIALS AND METHODS

Different Methods of Scatter Compensation

Five different methods of scatter compensation consisting of both scatter estimation and reconstruction-based scatter compensations were investigated and compared with the case of no scatter compensation in an attempt to improve detection for hot-activity lesions in ^{67}Ga citrate SPECT imaging. In this article, the specific approaches investigated are the following:

Perfect Scatter Rejection (PSR). Using a theoretical detector with a very good energy resolution, it is possible to eliminate most scattered photons from the photopeak projection data based solely on the detected photon energy. This is possible because the photopeak acquisition window can be made very narrow around the photopeak emission energies, whereas the scatter distribution remains quite broad over all energies. As a result, very few scattered photons will have the exact same energy as the photopeak photons and, hence, very few scattered photons will be collected within the photopeak energy windows. In using this method, we have assumed the best case scenario in which the theoretical detector has ideal energy resolution and thus only collects unscattered photons.

Ideal Scatter Compensation (ISC). This method utilizes a noise-free, mean photon scatter distribution at each projection angle. This scatter distribution is calculated via Monte Carlo simulation and would represent the ideal case, where the true mean scatter distribution of the true object activity at each projection angle is known. In the simplest approach, the scatter distribution can be presubtracted from the measured photopeak projection data before image reconstruction. When this is performed, one must be careful, however, to account for possible negatives present in the modified projection data. This type of implementation of scatter compensation is common in filtered backprojection, or other analytic reconstruction methods, but can also be used in iterative reconstructions. However, we have shown through human LROC studies that, when using this approach with the rescaled block iterative (RBI) reconstruction algorithm (*31*), lesion detectability may actually be reduced at clinical noise levels compared with making no compensation at all (*32*), as a result of subtracting noisy scatter estimates from noisy projection data. Therefore, when performing this type of scatter compensation using an iterative procedure, the following alternative strategy is recommended; rather than subtracting the scatter estimate from the projection data before image reconstruction, the scatter estimate is instead modeled into the projection step of the iterative reconstruction algorithm. Using the scatter estimate in this manner, there is no possibility of negative

values being present within the projection data as the scatter compensation is always an additive step.

A careful note must be made, however, in that the ISC method is not clinically feasible as it uses the true scatter distribution from the original Monte Carlo simulation at each projection angle. As such, this method should represent an upper limit on the accuracy of the scatter distribution estimates.

Triple-Energy Window (TEW). In this method, the scatter distribution within the photopeak window is estimated by acquiring additional energy windows adjacent to each photopeak (*8*). The number of scattered photons collected within each pixel of the photopeak window can then be estimated via the equation:

$$s_e = 0.5W_p\left[\frac{E_2}{W_2} + \frac{E_u}{W_u}\right],$$

where W_p represents the width of the photopeak window (in keV), E_2 and E_u are the number of counts in the 2 adjacent scatter windows, and W_2 and W_u are the widths of these respective windows. Note that this calculation is performed for each detector pixel at each projection angle. Since the scatter estimate calculated with this method will typically consist of noisy data, it is essential to apply a low-pass filter to these data to reduce the noise content before being included in the reconstruction process. The selection of the appropriate filter was the subject of an initial investigation and will be described in further detail along with details of the scatter windows used in this study. Once obtained, the low-pass–filtered scatter estimate is included in the projection step of iterative image reconstruction in an identical manner to the ISC method.

Effective Scatter Source Estimation (ESSE). This RBSC method uses a Monte Carlo derived scatter kernel to estimate the scatter contribution to the measured projection data of a given activity source distribution (*13*). This method uses the object-specific attenuation map and an estimated activity source distribution during the reconstruction process to calculate this scatter estimate. Scatter kernels used for this method are precalculated using the SIMIND Monte Carlo program (*33*) and simulate a point source of activity within a large water bath. Scatter kernels corresponding to the 93- and 185-keV photopeaks of ^{67}Ga were calculated and then averaged together for use in the reconstruction procedure.

Postreconstruction Scatter Subtraction (PRSS). This method reconstructs a scatter–activity distribution using the TEW-estimated scatter projection data. This distribution is then subtracted from the independently reconstructed photopeak projection data to yield a scatter-compensated activity distribution image. Again, estimated scatter projection data are initially low-pass filtered using the same filter as used in the TEW method.

Simulation Experiments

To test the effectiveness of the different scatter compensation methods, it was first necessary to create a SPECT projection dataset that incorporates photon scatter. For this, we have used the SIMIND Monte Carlo program (*31*) to simulate a SPECT acquisition of the mathematic cardiac-torso (MCAT) phantom (*34*). The biodistribution of ^{67}Ga citrate within this phantom was based on postmortem examinations of human subjects (*35*). A total of 450×10^6 emission photons from all photopeak energies were collected at each projection angle, thereby resulting in nearly noise-free projection data. Data were acquired from a 256^3-voxel representation of the MCAT phantom, into 128^2-projection matrices at 120 different projection angles encompassing 360°. Spherical lesions of 1-cm diameter were then placed at 300 different possible lesion locations within the mediastinal region of the phantom and SPECT projection data were simulated in a manner identical to that described for the background. Possible lesion locations were chosen under the consultation of a physician and were placed in clinically likely locations. Note that no photon interactions within the collimator were simulated at this point, although it is acknowledged that an appreciable amount of septal penetration and x-ray production will occur in clinical ^{67}Ga imaging. The inclusion of these effects is left to a later investigation as the goal at this point was to investigate solely the impact of photon scatter within the patient.

Projection data were acquired into a total of 9 energy windows consisting of a central photopeak window and 2 adjacent 8-keV wide-scatter windows for each of the 3 major, lower-energy photopeaks (Table 2). Primary photons (i.e., unscattered) were differentiated from scattered photons so that the true scatter distribution could be obtained for use in the ISC method as well as to provide a primary-only dataset to use for the PSR method. The simulated low-noise projection data were then rescaled to a total of 20 million collected photons within the acquired 93- and 185-keV energy windows (including the adjacent scatter windows). This number of counts was established based on similarly acquired clinical studies. Poisson distributed random noise was then added to these data. Datasets consisting of primary-only photons and primary + scattered photons were then created by summing the 93- and 185-keV energy windows together as is routinely performed in clinical acquisitions. At this point, the photopeak data for the primary-only dataset contained a total of about 8.5 million counts, whereas the primary + scatter datasets contained 20 million counts total (14.8 million within the photopeaks, 5.2 million in the scatter windows). Note that while the 300-keV photopeak window was simulated and acquired, subsequent image reconstructions did not take advantage of this additional energy window. This was due to the fact that we wanted the simulation to closely match our current clinical practice, which, due to various hardware limitations, does not use this higher-energy window.

Image reconstructions were performed using the RBI algorithm (*31*) with 4 angles per subset and with each scatter compensation method. Compensations for 3-dimensional (3D) detector response and object-specific attenuation were included. Object-specific attenuation maps were obtained using a simulated ^{99m}Tc moving line source with a clinically relevant number of transmission photons (*36*). Attenuation maps were reconstructed using 30 iterations of the BITAB algorithm (*37*) and low-pass filtered with a 3D gaussian filter with a FWHM of 0.6 cm as had been determined previously (*36*). The same attenuation map was used for all reconstruction methods to maintain consistency among strategies.

TABLE 2
Acquisition Energy Windows Used in Simulation Experiment

Photopeak window (keV)	Lower-scatter window (keV)	Upper-scatter window (keV)
87–102	73–81	105–113
171–198	160–168	202–210
278–323	260–268	333–341

Only the first 2 energy windows were used for image reconstruction.

Optimization of Reconstruction Parameters

To determine optimal TEW filtering parameters, 6 different lesion locations were used with a lesion contrast of 15:1 using the signal-known- exactly, but variable CHO (SKEV-CHO). Image reconstructions were performed with the TEW scatter compensation method using 2 reconstruction iterations with the same postreconstruction filter. A range of Butterworth prefiltering parameters was applied to the scatter projection data to determine the optimal filter order and cutoff frequency. For each location, the SKEV-CHO evaluates the signal-to-noise ratio, d′, and converts it into an A_z. The A_z values were then averaged over the 6 lesion locations to formulate an overall detectability score along with a measurement of SE. The approximate optimal reconstruction parameters are found from the maximum value on the A_z versus filter parameter plot.

After TEW filter parameters were established, the same SKEV-CHO model was used to evaluate the approximate number of iterations and postreconstruction filtering required for optimal lesion detection when using each scatter compensation reconstruction method. Reconstructions were performed using from between 1 and 4 iterations and with postreconstruction filtering using a 3D gaussian filter with FWHM values ranging from 1 to 4 voxels.

Using the estimated optimal reconstruction parameters obtained from the SKEV-CHO model, a follow-up human observer LROC study was performed to determine the relative effectiveness of the various scatter compensation methods in reducing scatter effects and improving lesion detection. In a typical SKE-ROC study, a human observer must assess several identically reconstructed images as to the likelihood of a lesion being present at a specific location. In LROC, the observer not only must supply a confidence rating as to the likelihood of a lesion being present but also must localize the lesion within the image. In the LROC user interface used, an image is shown to the observer who then proceeds to select the likely lesion location in the image via a crosshair controlled by a computer mouse. The observer must then supply a confidence rating on the likelihood of a lesion being present at the selected location. After the evaluation of several images reconstructed with a given strategy, an overall detectability can be calculated.

For this LROC study, 5 observers from the Medical Physics Group at the University of Massachusetts Medical School participated. Twelve different image sets were read by each observer, with each image set consisting of 150 images. For all strategies, a postreconstruction gaussian filter with a FWHM equal to 3 voxels (1.25 cm) was used as it was determined from the SKEV-CHO studies that this was nearly optimal under most conditions.

Within each image set, images were divided into an initial training group of 48 images, followed by the study group of 102 images. Within each group, half of the displayed images did not contain a lesion, whereas the other half consisted equally of low-, mid-, and high-contrast lesions (20:1, 25:1, and 30:1). For each image shown, the observers were asked to select the most likely lesion location via a movable crosshair controlled by a computer mouse and to provide a confidence rating that the lesion is present on a discrete scale ranging from 1 (confident, no lesion present) to 6 (confident, lesion present). During the training, observers were given feedback as to the truth regarding lesion presence and location after recording their confidence score. No feedback was supplied to the observer when reading the actual test images, and only rating data for these images were used in the subsequent assessment of lesion detectability. Identical lesion locations were used for each image set, and each image set was read in the same order by the observers. However, the ordering of the images for each reconstruction strategy was different, thereby reducing some of the reading-order effects.

After the reading of an entire image set, LROC observer data were evaluated in terms of localization accuracy. We have previously shown that most lesions are correctly localized to within 9 display pixels (i.e., 1.87 cm) of their true location (*1*,*38*), so we have chosen this as the cutoff distance between calling localization correct or incorrect. Once data have been ordered as to correct lesion location and confidence rating, they are then entered into an LROC data-fitting program (*39*). This fitting program determines the lesion detectability of each strategy by evaluating the area-under-the-LROC-curve (A_{LROC}) and the probability of correct localization (P_L). The A_{LROC} values were analyzed using 2-way ANOVA to determine if there were any statistically significant differences among reconstruction strategies or observers. If a significant difference was indicated, then the Scheffé nonparametric multiple comparison test was used to determine which methods were significantly different.

In previous studies involving ^{67}Ga SPECT, we have seen that the SKEV-CHO correlates very well with human LROC observer data (*22*). These previous studies, however, have used simulated SPECT images that did not model photon scatter. Additionally, the numerical observer used in these previous studies was a signal-known-exactly type and thus the task associated with this type of numerical observer is not the same as that performed by the human observers in an LROC study. An additional concern of relying solely on the SKEV-CHO as a method to optimize and evaluate each image reconstruction method was the fact that the wide range of A_z values obtained for each lesion location and the subsequent averaging of these scores to obtain an overall detectability results in an error measurement on each value that was rather large, thereby reducing our statistical ability to differentiate reconstruction strategies. For these reasons, we have used a different type of numerical observer that is based on human perception studies and follows the methodology of human observer LROC (*24*,*25*). This observer will be denoted as a CNPW observer. We have applied this observer to the same image sets that were evaluated by the human observers during the LROC study to determine the extent to which it would be able to predict the relative rankings of the scatter compensation strategies compared with the human observers and thus validate its use as a possible replacement for human LROC.

We will denote a single noisy 3D reconstruction by the variable **f**. Different postreconstruction image processing will be performed on this dataset before being displayed to an observer. This processing includes filtering, slice extraction, adaptive thresholding, byte scaling, and interpolating to 256 × 256 display pixels. We will denote all of these postprocessing operations by the operator S. As a result of these operations, an image displayed to an observer can be denoted by the operation S**f**.

When scoring an image during an LROC session, a human observer must supply the coordinates of the most likely lesion location, r_t, as well as the confidence rating, λ, as to the presence of a lesion at that location. These data come about through the evaluation of a series of latent perception measurements, Z(r), made at several locations within each image. In human studies, this measurement is made by comparing the image signal at a given location to an internally perceived lesion signal. In the CNPW numerical observer analog, these perception measurements are the result of a 2-dimensional (2D) cross-correlation of a given test

image with a predefined signal kernel. This signal kernel is equal to a channelized version of the mean lesion signal present—that is, the kernel is equal to the mean lesion signal, s(r), passed through a series of selective observer template channels such that:

$$\omega_{npw}(r) = \bar{s}(r),$$

or on channelizing this signal:

$$\omega_{cnpw}(r) = \sum_{i=1}^{C} \langle u_i, \bar{s} \rangle u_i(r),$$

where C represents the number of observer channels used and u_i represents the *i*th bandpass channel. In this study, we have used 3 square-profile frequency-bandpass channels, as has been done in the past for the SKEV-CHO. The determination of the perception measurement is then equal to:

$$Z(r) = \omega_{CNPW} \otimes [S(\boldsymbol{f} - \bar{\boldsymbol{b}})],$$

where $\boldsymbol{f}$ represents the reconstructed image data under consideration, and $\bar{\boldsymbol{b}}$ represents the mean, lesion-absent background image. In this implementation, we have chosen to substitute the noise-free background $\hat{\boldsymbol{b}}$ rather than the mean background to reduce computational burden.

As described, the CNPW observer denotes the location of the lesion using the maximum value of the latent perception measurement within a search region Ω. The search region used corresponds to a 2D region that encompasses the possible tumor locations within each slice. In this way, the observer would not be misled by high-activity regions such as the liver outside the region of possible lesion sites. To provide the rating data, λ, we have chosen to use the raw latent perception measurement value at the determined lesion location. Thus, the lesion location and rating can be written as:

$$r_l = \arg\max_{r \in \Omega} Z(r),$$

$$\lambda = Z(r_l).$$

After all images in a given study set are rated, the continuous rating data are then converted into 1 of 6 discrete rating scores based on a linear scaling of the range of continuous observer rating data. Other conversion functions have also been tested (e.g., logarithmic conversions), but results thus far appear very similar among conversion functions.

Values corresponding to the lesion locations, r_l, and confidence ratings, λ, are then input into the same LROC fitting program as used for human studies to obtain LROC curves and subsequent A_{LROC} values for each reconstruction strategy. Using this model observer, optimization of image reconstruction parameters such as number of iterations and amount of postreconstruction filtering could be performed relatively quickly compared with human LROC studies and the SKEV-CHO, provided that reconstructed image sets are already available.

RESULTS

The role of the SKEV-CHO in this investigation was to determine the optimal prefiltering of the TEW scatter estimate and to estimate the approximate reconstruction parameters required for optimal lesion detection. For the TEW filtering optimization, 6 different lesion locations were used with varying filter parameters, whereas a total of 30 different lesion locations were used in the determination of reconstruction parameters. In all cases, lesion-to-background contrast was preset at 15:1. The SKEV-CHO yielded an A_z value for each lesion location for a given reconstruction strategy. Aggregate scores for each reconstruction method were calculated by averaging together all locations and are reported along with the associated SE measurement.

In the initial optimization of TEW filtering parameters, it was found that maximal lesion detection occurs when the TEW scatter estimate was prefiltered with a Butterworth filter of order 4 and cutoff of around 0.15 cycle/cm. Plots of the A_z versus filter cutoff are shown in Figure 2. Results of this plot agree consistently with previous studies that evaluated mean-square-error (MSE) and concluded that prefiltering the TEW scatter estimate with a Butterworth filter with a cutoff between 0.10 and 0.20 cycle/cm minimized the MSE between the true image and the reconstructed image (*40*). Note, however, the compactness of the the *y*-axis (range, 0.90–0.92). This is typical of SKEV-CHO in the fact that the variation in A_z values is typically quite small. For this reason it was believed that the statistical power of differentiating between methods based solely on SKEV-CHO may be problematic.

In Figure 3, SKEV-CHO plots are shown for 5 of the reconstruction strategies consisting of PSR, no scatter compensation (NoSC), ISC, TEW, and ESSE. Again, note the relative compactness of the *y*-axis ranges (0.95–0.97 for

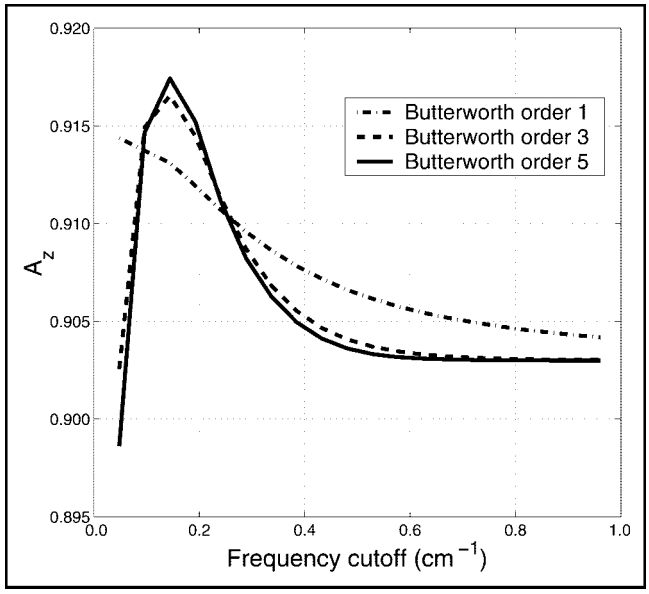

FIGURE 2. Results of SKEV-CHO depicting average A_z values as a function of Butterworth cutoff frequency and order for TEW scatter estimation prefiltering. SEs, not shown on these plots, were between 0.01 and 0.02. All reconstructions were performed with 2 RBI reconstruction iterations and a postreconstruction filter using 2-voxel FWHM 3D gaussian. Maximal scores are obtained using a Butterworth filter with order 5 and cutoff of ~0.15 cm^{-1}.

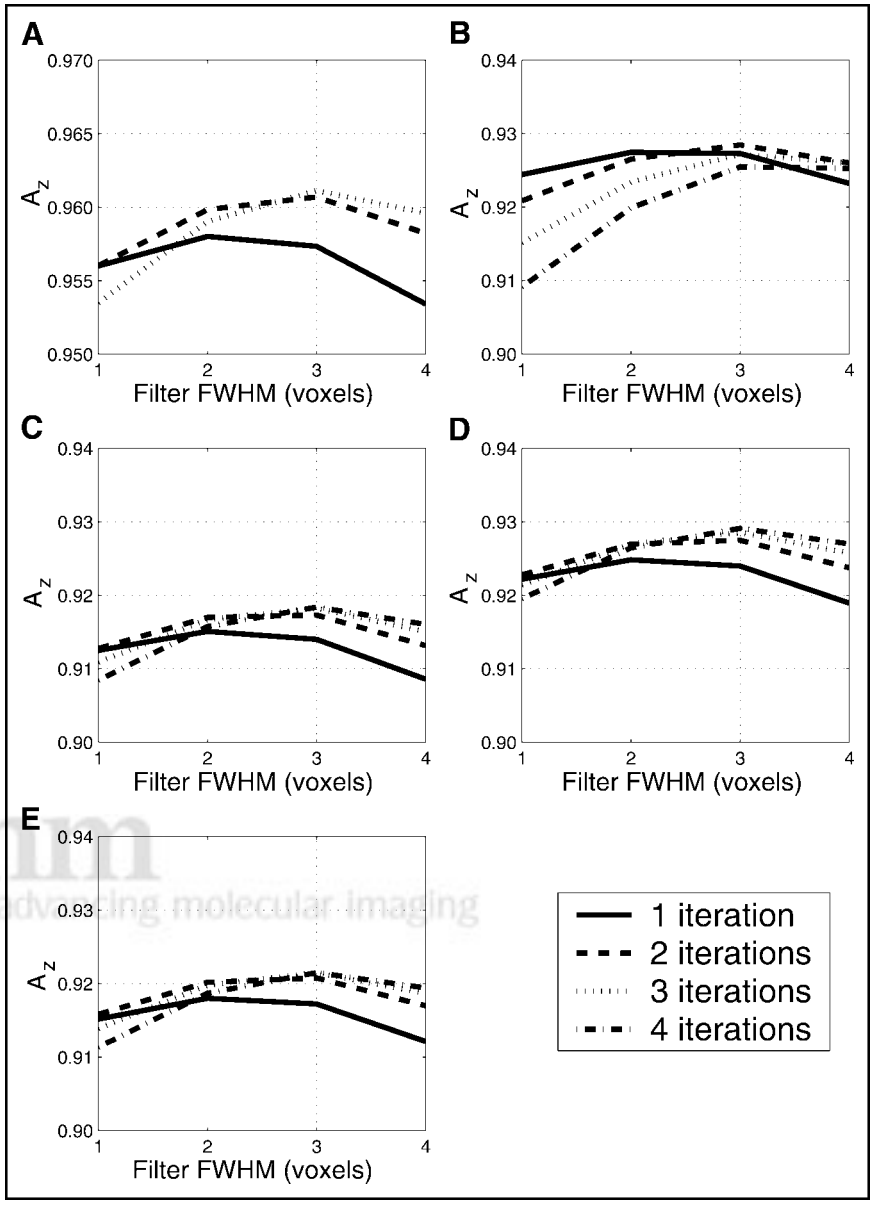

FIGURE 3. SKEV-CHO scores vs. postreconstruction filter size and iteration number for 5 different reconstruction strategies. Methods consist of PSR (A), no scatter compensation (NoSC) (B), ISC (C), TEW compensation (D), and ESSE (E). Note different *y*-axis scale used for case of PSR. SEs at each data point were equal to about 0.01.

PSR, 0.90–0.94 for the other methods). Again, due to the small variation in A_z values between methods, it was thought that a comparison between reconstruction strategies may be problematic. The postreconstruction scatter subtraction (PRSS) method was not tested with the SKEV-CHO as it is not immediately evident how to implement the subtraction step into the low-noise approximations used in the current implementation. As a result, reconstruction parameters for this method have been estimated based on results from the other reconstruction strategies.

Optimal lesion detection occurs when the A_z values for the SKEV-CHO are at a maximum. From Figure 3, it appears that this maximum point occurs when performing between 2 and 4 reconstruction iterations and with 3D postreconstruction filtering with a FWHM of about 3 voxels. Based on these findings, image sets for the subsequent human LROC study consisted of images reconstructed with both 2 and 4 iterations and with a postreconstruction filter of 3 voxels FWHM.

Sample images of each reconstruction strategy are shown in Figure 4. Based on visual examination of these images, it appears as though the different scatter compensation strategies reduce the influence of scattered photons on the reconstructed images compared with the case of no compensation, thereby possibly yielding greater contrast between the lesion and the background. Not surprisingly, the PSR images appear to have the greatest contrast between the lesion and the background, whereas the NoSC images appear to have the worst. Also note that the PRSS method appears to produce a "halo" effect of low-activity regions near areas with increased activity, such as around the ribs and spine. This is presumed to be due to the fact that the

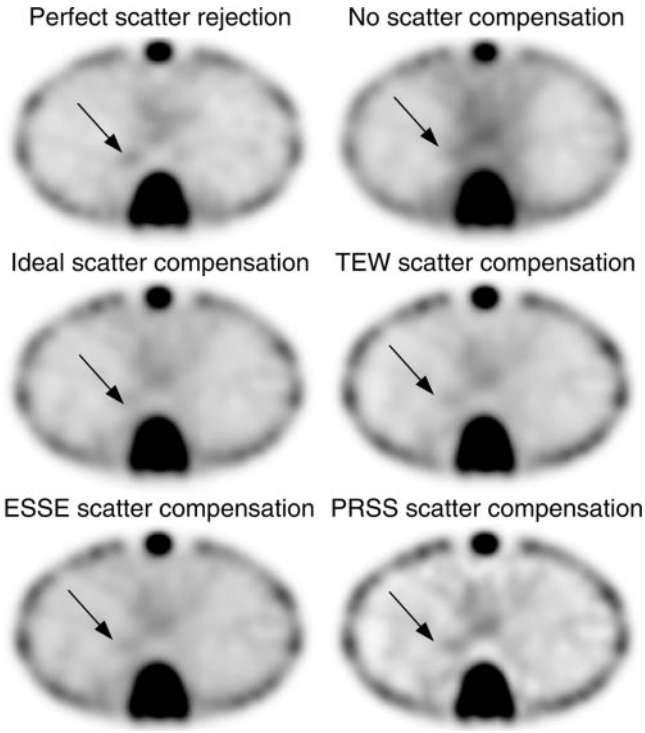

FIGURE 4. Sample reconstructions using different scatter compensation strategies outlined. Four iterations of RBI algorithm were used with 4 angles per subset. Same transverse slice is shown for all strategies. Arrow indicates location of a simulated lesion.

reconstructed scatter activity distribution is very similar to a heavily smoothed image of the photopeak activity distribution and, therefore, the subtraction of the scatter image from the photopeak image acts like an unsharp-masking operation, yielding somewhat sharper definition in certain structures. The effect on this operation on hot-activity lesions is not immediately known but will be determined via the LROC observer studies.

Results from the human LROC observer study are shown in Table 3, in which A_{LROC} values are reported at both 2 and 4 reconstruction iterations. To compare reconstruction strategies to test for statistical differences, 2-way ANOVA was first performed. The results are given in Table 4. As can be seen, significant differences are present between scatter compensation methods and, to a lesser degree, between different observers. To determine which methods are statistically different, a follow-up Scheffé multiple comparison significance test was performed. The result of this comparison test is given in Table 5.

TABLE 4
Results of 2-Way ANOVA for Human LROC Study

Source of variation	Sum of squares	df	Mean square	f	P
Between methods	0.081	5	0.016	16.16	0.00
Between observers	0.017	4	0.004	4.13	0.01
Error	0.020	20	0.001		
Total	0.118	29	0.004		

df = degrees of freedom.

DISCUSSION

From these results, it is seen that the inclusion of scatter compensation, particularly TEW or ESSE, appears to improve lesion localization and detectability over NoSC. However, no method is able to achieve the same degree of performance as the PSR method. This is not surprising as the PSR method eliminates scattered photons from the acquired data altogether and so does not make any approximations during the reconstruction process. PSR also does not lead to any noise amplification as other methods will because the actual scatter contribution to the projections is a stochastic variable that the compensation strategies try to correct deterministically. A more surprising result from this study, however, is the fact that ISC does not perform statistically significantly better then NoSC, whereas approximate methods such as TEW and ESSE do. Perhaps this indicates that an additional image enhancement is occurring in TEW and ESSE reconstruction that makes lesion localization easier, thereby resulting in improved A_{LROC} scores.

We next compared the reconstruction strategies using our newly developed numerical observer to determine the extent to which it could predict the relative rankings of the human observers. Using this observer, we are able to efficiently perform analysis using a much wider range of reconstruction parameters than when performing human LROC studies. In these numerical observer studies, we therefore have used the numerical observer with images reconstructed with between 2 and 8 reconstruction iterations and with postre-

TABLE 3
Average Human Observer A_{LROC} Values for 6 Different Scatter Compensation Methods Tested

Iterations	Scatter compensation method					
	PSR	NoSC	ISC	TEW	ESSE	PRSS
2	0.84 ± 0.01	0.67 ± 0.02	0.69 ± 0.02	0.72 ± 0.02	0.73 ± 0.02	0.72 ± 0.03
4	0.83 ± 0.01	0.66 ± 0.02	0.70 ± 0.02	0.75 ± 0.02	0.73 ± 0.03	0.71 ± 0.03

Errors = the SE over 5 observers.

TABLE 5
Significance Values (*P*) Obtained from Scheffé Multiple Comparison Test on 6 Different Scatter Compensation Strategies Obtained from Human LROC Studies

	Scatter compensation method					
Strategy	PSR	NoSC	ISC	TEW	ESSE	PRSS
PSR	—					
NoSC	**0.00**	—				
ISC	**0.00**	0.30	—			
TEW	**0.00**	**0.02**	0.22	—		
ESSE	**0.00**	**0.03**	0.26	1.00	—	
PRSS	**0.00**	0.08	0.79	0.73	0.79	—

Values in boldface represent significant differences at $P < 0.05$ level.

construction low-pass filtering of using a 3D gaussian filter with a FWHM ranging from 0 to 6 voxels. Figure 5 depicts the results of the numerical observer studies using the 6 different reconstruction strategies. This was again followed by a Scheffé multiple comparison test to compare the different scatter compensation strategies (Table 6). Similar trends are seen in these plots for the A_{LROC} as was seen in the human observer LROC study—that is, all methods of scatter compensation that were tested improve lesion detection compared with NoSC; however, even the best method (TEW) falls short of achieving similar A_{LROC} scores as that which is obtained when no scattered photons are acquired at all (maximum scores, 0.76 vs. 0.90). In a very similar manner to the human results, the ISC performs only marginally better than using no scatter compensation (maximum scores, 0.70 vs. 0.69). With the exception of the ISC, which prefers a higher number of reconstruction iterations, one can see that either 2 or 4 iterations of RBI, followed by

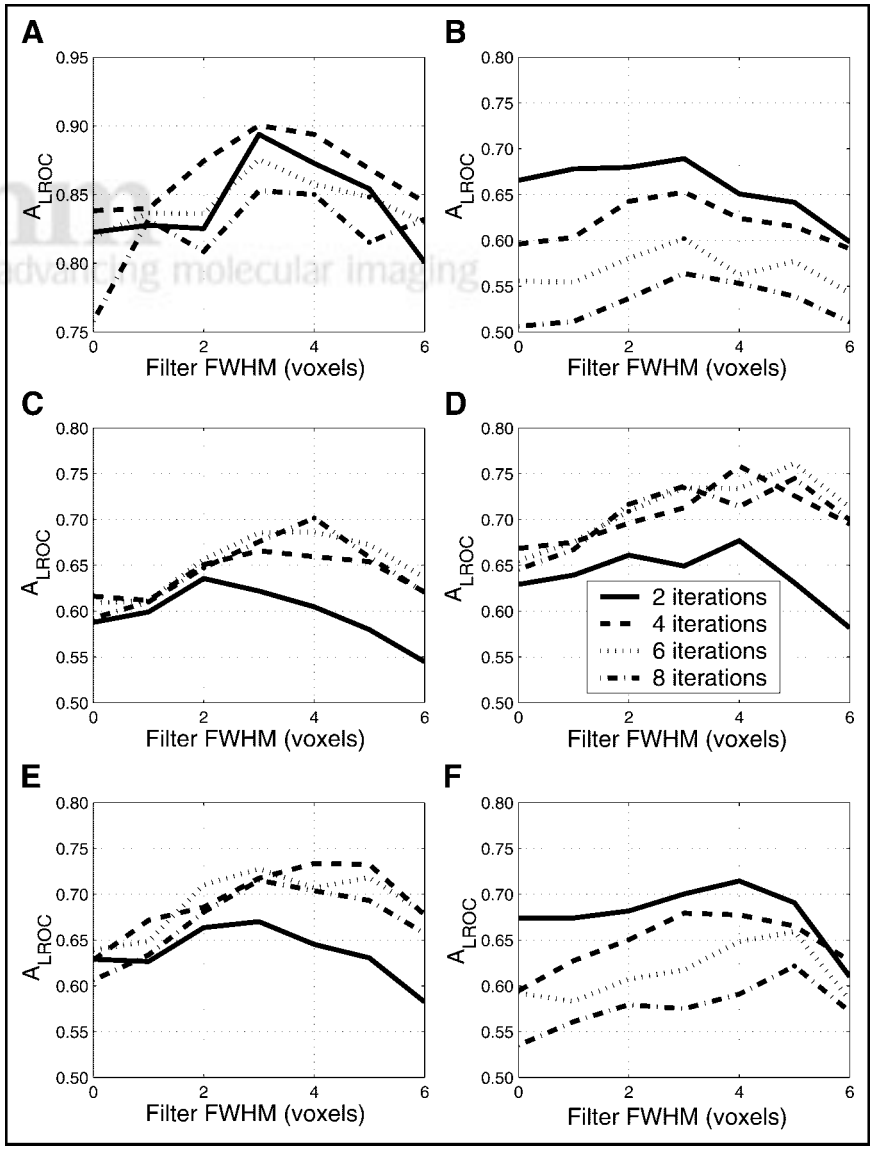

FIGURE 5. Results of CNPW numerical observer for different reconstruction strategies consisting of PSR (A), NoSC (B), ISC (C), TEW compensation (D), ESSE (E), and PRSS (F). Errors bars equal to about 0.02 for each data point are not shown.

a 3D postreconstruction filter of width 3 voxels FWHM was at or near the peak of the A_{LROC} curves. This confirms that the selection of human observer reconstruction parameters was close to ideal and, in all likelihood, different parameters would not have resulted in significantly different conclusions regarding the relative performances of the various scatter compensation methods.

In light of the similarities between the numerical LROC observer results and the human LROC study, a Spearman rank order test was performed to evaluate the correlation between the human LROC observer study and the LROC numerical observer. The scatter plot comparing the LROC numerical observer and human observers doing an LROC task are shown in Figure 6. The calculated Spearman rank order coefficient (r_s) was 0.74, thus indicating that this numerical observer models human observers fairly well for the reconstructed strategies tested.

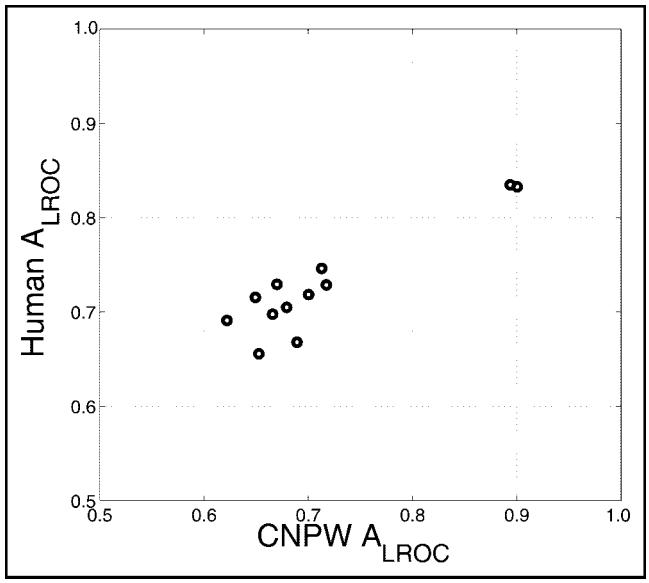

FIGURE 6. Observer correlations between human LROC studies and proposed LROC numerical observer (Spearman rank order coefficient, $r_s = 0.74$).

CONCLUSION

The inclusion of scattered photons in ^{67}Ga citrate imaging significantly degrades human observer lesion detection. In an effort to improve lesion detectability, different reconstruction strategies using scatter compensation have been investigated and compared with the NoSC case. The methods tested represent a range of ideal and clinically useful methods and indicate that some improvement can be made to lesion detectability with scatter compensation strategies such as TEW or ESSE. However, it is also important to note that some additional noise blobs are often seen in scatter-compensated images that may make the detection of lesions more difficult. Somewhat surprising is the result that the ISC does not perform much better than applying NoSC. However, it must be pointed out that this conclusion is the result of a lesion detection task and may not be indicative of other tasks such as activity quantitation.

In an effort to better model human LROC observers, we have investigated the use of a numerical LROC observer. This observer uses identical LROC image sets as the human observers and has been shown to correlate well with LROC studies, thus indicating that it is a good predictor of human detection performance in ^{67}Ga citrate imaging.

TABLE 6
Significance Values (*P*) Obtained From Scheffé Multiple Comparison Test of Numerical Observer LROC Studies

	Scatter compensation method					
Strategy	PSR	NoSC	ISC	TEW	ESSE	PRSS
PSR	—					
NoSC	**0.00**	—				
ISC	**0.00**	**0.00**	—			
TEW	**0.00**	**0.00**	**0.00**	—		
ESSE	**0.00**	**0.00**	0.20	0.80	—	
PRSS	**0.00**	0.47	0.32	**0.00**	**0.00**	—

Values in boldface represent significant differences at $P < 0.05$ level.

ACKNOWLEDGMENTS

The authors acknowledge the advice and encouragement of Dr. Charles E. Metz, Dr. Harrison H. Barrett, and Dr. Philip F. Judy in the development of the observer methods used in this investigation. This work has been supported by the National Institute for Biomedical Imaging and Bioengineering (NIBIB) under grant EB-002798. Its contents are solely the responsibility of the authors and do not necessarily represent the official views of the NIBIB.

REFERENCES

1. Farncombe TH, Gifford HC, Narayanan MV, et al. An optimization of reconstruction parameters and investigation into the impact of photon scattering Ga-67 SPECT. *IEEE Trans Nucl Sci.* 2002;49:2148–2154.
2. Jaszczak RJ, Coleman RE, Whitehead FR. Physical factors affecting quantitative measurements using camera-based single photon emission computed tomography (SPECT). *IEEE Trans Nucl Sci.* 1981;28:69–80.
3. Jaszczak RJ, Whitehead FR, Lim CB, Coleman RE. Lesion detection with single photon emission computed tomography (SPECT) compared with conventional imaging. *J Nucl Med.* 1982;23:97–102.
4. Beekman FJ, Kamphuis C, Frey EC. Scatter compensation methods in 3D iterative SPECT reconstruction: a simulation study. *Phys Med Biol.* 1997;42: 1619–1632.
5. Kadrmas DJ, Frey EC, Tsui BMW. Application of reconstruction-based scatter compensation to thallium-201 SPECT: implementations for reduced reconstructed image noise. *IEEE Trans Med Imaging.* 1998;17:325–333.
6. Jaszczak RJ, Greer KL, Floyd CE, Harris CC, Coleman RE. Improved SPECT quantitation using compensation for scattered photons. *J Nucl Med.* 1984;25: 893–900.
7. Msaki P, Axelson B, Dahl CM, Larsson SA. Generalized scatter correction method in SPECT using point scatter distribution functions. *J Nucl Med.* 1987; 28:1861–1869.
8. Ogawa K, Harata Y, Ichihara T, Kubo A, Hashimoto S. A practical method for

position-dependent Compton-scatter correction in single photon emission CT. *IEEE Trans Med Imaging.* 1991;10:408–412.
9. Bowsher JE, Johnson VA, Turkington TG, Jaszczak RJ, Floyd CE, Coleman RE. Bayesian reconstruction and use of anatomical a priori information for emission tomography. *IEEE Trans Med Imaging.* 1996;15:673–686.
10. Floyd CE, Jaszczak RJ, Coleman RE. Inverse Monte Carlo: a unified reconstruction algorithm. *IEEE Trans Nucl Sci.* 1985;32:785–799.
11. Welch A, Gullberg GT, Christian PE, Datz FL. A transmission map-based scatter correction technique for SPECT in inhomogeneous media. *Med Phys.* 1995;22: 1627–1635.
12. Beekman FJ, Kamphuis C, Viergever MA. Improved SPECT quantitation using fully three-dimensional iterative spatially variant scatter response compensation. *IEEE Trans Med Imaging.* 1996;15:491–499.
13. Frey EC, Tsui BMW. A new method for modeling the spatially variant, object-dependent scatter response function in SPECT. *IEEE Nucl Sci Symp Med Imaging Conf Rec.* 1996;2:1082–1086.
14. Gagnon D, Todd-Pokropek A, Arsenault A, Dupras G. Introduction to holospectral imaging in nuclear medicine for scatter subtraction. *IEEE Trans Med Imaging.* 1989;MI-8:245–250.
15. El Fakhri GN, Moore SC, Maksud P. A new scatter compensation method for Ga-67 imaging using artificial neural networks. *IEEE Trans Nucl Sci.* 2001;48: 799–804.
16. Beekman FJ, deJong HWAM, Slijpen ETP. Efficient SPECT scatter calculation in non-uniform media using correlated Monte Carlo simulation. *Phys Med Biol.* 1999;44:N183–N192.
17. deJong HWAM, Slijpen ETP, Beekman FJ. Acceleration of Monte Carlo SPECT using convolution-based forced detection. *IEEE Trans Nucl Sci.* 2001;48:58–64.
18. Wells RG, Celler A, Harrop R. Experimental validation of an analytical method of calculating SPECT projection data. *IEEE Trans Nucl Sci.* 1997;44:1283–1290.
19. Kamphuis C, Beekman FJ, van Rijk PV, Viergever MA. Dual matrix ordered subsets reconstruction for accelerated 3D scatter compensation in single-photon emission tomography. *Eur J Nucl Med.* 1998;25:8–18.
20. Zeng GL, Bai C, Gullberg GT. A projector/backprojector with slice-to-slice blurring for efficient three-dimensional scatter modeling. *IEEE Trans Med Imaging.* 1999;18:722–732.
21. Beekman FJ, deJong HWAM. Efficient fully 3D iterative SPECT reconstruction with Monte Carlo-based scatter compensation. *IEEE Trans Med Imaging.* 2002; 21:867–877.
22. de Vries DJ, King MA, Soares EJ, Tsui BMW, Metz CE. Evaluation of the effect of scatter correction on lesion detection in hepatic SPECT imaging. *IEEE Trans Nucl Sci.* 1997;44:1733–1740.
23. de Vries DJ, King MA, Soares EJ, Tsui BMW, Metz CE. Effects of scatter subtraction on detection and quantitation in hepatic SPECT. *J Nucl Med.* 1999; 40:1011–1023.
24. Metz CE. Some practical issues of experimental design and data analysis in radiological ROC studies. *Invest Radiol.* 1989;24:234–245.
25. Wells RG, King MA, Simkin PH, et al. Comparing filtered backprojection and ordered-subsets expectation maximization for small-lesion detection and localization in Ga-67 SPECT. *J Nucl Med.* 2000;41:1391–1399.
26. Gifford HC, King MA, Wells RG, Hawkins WG, Narayanan MV, Pretorius PH. LROC analysis of detector-response compensation in SPECT. *IEEE Trans Med Imaging.* 2000;19:463–473.
27. Gifford HC, Wells RG, King MA. A comparison of human observer LROC and numerical observer ROC for tumor detection in SPECT images. *IEEE Trans Nucl Sci.* 1999;46:1032–1037.
28. Soares EJ, Byrne CL, Glick SJ. Noise characteristics of block-iterative reconstruction algorithms. I. Theory. *IEEE Trans Med Imaging.* 2000;19:261–270.
29. Gifford HC, Farncombe TH, King MA. Ga-67 tumor detection using penalized-EM with nonanatomical regularizers. *IEEE Nucl Sci Symp Med Imaging Conf Rec.* 2002;3:1397–1401.
30. Gifford HC, Pretorius PH, King MA. Comparison of human- and model-observer LROC studies. *Proc SPIE.* 2003;5034:112–122.
31. Byrne CL. Block-iterative methods for image reconstruction from projections. *IEEE Trans Imaging Proc.* 1996;5:792–794.
32. Farncombe TH, Gifford HC, Narayanan MV, King MA. A comparison of triple energy window scatter compensation methods for Ga-67 tumor imaging [abstract]. *J Nucl Med.* 2002;43(suppl):54P.
33. Ljungberg M, Strand SE. A Monte Carlo program for the simulation of scintillation camera characteristics. *Comput Methods Programs Biomed.* 1989;29:257–272.
34. Tsui BMW, Terry JA, Gullberg GT. Evaluation of cardiac cone-beam single photon emission computed tomography using observer performance experiments and receiver operating characteristics analysis. *Invest Radiol.* 1993;28:1101–1112.
35. Nelson B, Hayes RL, Edwards CL, Kniseley RM, GA Andrews. Distribution of gallium in human tissues after intravenous administration. *J Nucl Med.* 1972;13: 92–100.
36. Wells RG, Gifford HC, Pretorius PH, Farncombe TH, King MA. The impact of noisy and misaligned attenuation maps on human-observer performance at lesion detection in SPECT. *IEEE Trans Nucl Sci.* 2002;49:753–760.
37. Narayanan MV, Byrne CL, King MA. An interior point iterative maximum-likelihood reconstruction algorithm incorporating upper and lower bounds with application to SPECT transmission imaging. *IEEE Trans Med Imaging.* 2001; 20:342–353.
38. Wells RG, Simkin PH, Judy PF, et al. Maximizing the detection and localization of Ga-67 tumors in thoracic SPECT MLEM (OSEM) reconstructions. *IEEE Trans Nucl Sci.* 1999;46:1191–1198.
39. Swensson RG. Unified measurement of observer performance in detecting and localizing target objects on images. *Med Phys.* 1996;23:1709–1725.
40. King MA, deVries DJ, Pan TS, Pretorius PH, Case JA. An investigation of the filtering of TEW scatter estimates used to compensate for scatter with ordered subset reconstructions. *IEEE Trans Nucl Sci.* 1997;44:1140–1145.